Check for updates

Designing functionalized nanodiamonds with hyaluronic acid–phospholipid conjugates for enhanced cancer cell targeting and fluorescence imaging capabilities†

Sofia Sturari,‡[a,b] Ilaria Andreana,‡[c] Pietro Aprà, [b] Valeria Bincoletto,[d] Joanna Kopecka,[e] Lorenzo Mino, [d,f] Beatrice Zurletti,[c] Barbara Stella,[c] Chiara Riganti,[e] Silvia Arpicco*[c] and Federico Picollo [*a,b,d]

Nanomedicine aims to develop smart approaches for treating cancer and other diseases to improve patient survival and quality of life. Novel nanoparticles as nanodiamonds (NDs) represent promising candidates to overcome current limitations. In this study, NDs were functionalized with a 200 kDa hyaluronic acid–phospholipid conjugate (HA/DMPE), enhancing the stability of the nanoparticles in water-based solutions and selectivity for cancer cells overexpressing specific HA cluster determinant 44 (CD44) receptors. These nanoparticles were characterized by diffuse reflectance Fourier-transform infrared spectroscopy, Raman spectroscopy, and photoluminescence spectroscopy, confirming the efficacy of the functionalization process. Scanning electron microscopy was employed to evaluate the size distribution of the dry particles, while dynamic light scattering and zeta potential measurements were utilized to evaluate ND behavior in a water-based medium. Furthermore, the ND biocompatibility and uptake mediated by CD44 receptors in three different models of human adenocarcinoma cells were assessed by performing cytofluorimetric assay and confocal microscopy. HA-functionalized nanodiamonds demonstrated the advantage of active targeting in the presence of cancer cells expressing CD44 on the surface, suggesting higher drug delivery to tumors over non-tumor tissues. Even CD44-poorly expressing cancers could be targeted by the NDs, thanks to their good passive diffusion within cancer cells.

Introduction

Although it took approximately three decades from their first synthesis in the 1960s for nanodiamonds (NDs) to capture the interest of researchers, once they gained attention in the late 1990s, the fascination with these nanoparticles not only endured, but also steadily intensified.[1] As a result, a wide variety of methods for their production has been developed, encompassing both top-down approaches, like detonation of carbon-containing explosives[1,2] and grinding of High-Pressure High-Temperature (HPHT) microdiamond powders,[3] and bottom-up techniques, such as Chemical Vapor Deposition (CVD)[4] and synthesis from adamantane derivatives.[5] Similarly, an extensive array of post-synthetic procedures, including treatments with microwave plasma,[6,7] high-temperature thermal processes in controlled environments[8–10] and wet chemistry-based strategies,[11–13] have been established. This combined spectrum of synthesis methods and subsequent modifications enables the creation of NDs with diverse sizes, covering the 5–300 nm range, morphologies, and surface characteristics. These find applications in a rich landscape of fields, which includes tribology,[14,15] nanocomposites,[16,17] energy-related technologies,[18,19] sensing[20,21] and photonics,[22,23] thanks to their unique combination of physical and chemical properties.

In particular, due to their remarkable chemical stability and biocompatibility,[24] NDs stand out in the biomedical field, where they have been investigated as drug delivery systems,[25,26] additives in tissue scaffolds and surgical implants,[27,28] biosensors[29,30] and radiosensitizers.[31–33] In this context, they have also been extensively employed as fluo-

[a] Department of Physics, University of Torino, via P. Giuria 1, 10125 Torino, Italy. E-mail: federico.picollo@unito.it

[b] National Institute of Nuclear Physics, Sect. Torino, via P. Giuria 1, 10125 Torino, Italy

[c] Department of Drug Science and Technology, University of Torino, via P. Giuria 9, 10125 Torino, Italy. E-mail: silvia.arpicco@unito.it

[d] NIS Inter-Departmental Centre, via G. Quarello 15/a, 10135 Torino, Italy

[e] Department of Oncology, University of Torino, Piazza Nizza 44, 10126 Torino, Italy

[f] Department of Chemistry, University of Torino, via P. Giuria 7, 10125 Torino, Italy

†Electronic supplementary information (ESI) available. See DOI: https://doi.org/10.1039/d4nr00932k

‡Co-first authors.

rescent cellular biomarkers,[34–36] owing to their fluorescence properties arising from the presence of optically active lattice defects, such as Nitrogen-Vacancy (NV) centers, which show an intense photoluminescence in the red wavelength range when excited with a green laser.[37] Notably, the emission from NV centers is highly stable and resistant to quenching or photobleaching,[38–40] setting NDs apart from organic fluorophores, thus providing a significant advantage for their use in optical bioimaging. As a result, NDs have emerged as a promising tool for the visualization of cancer cells, relying on their preferential accumulation in tumor tissues, thanks to the Enhanced Permeation and Retention (EPR) effect.[41]

Moreover, to improve selectivity, thus enhancing ND uptake and internalization in cancer cells, active targeting can be accomplished through surface functionalization, which involves decorating the ND surface with specific molecules, acting as ligands that bind to overexpressed receptors on cancer cells or tumour vasculature.[42] Examples of this approach, typically grounded in covalent bond formation with the functionalizing moiety, comprise linking with antibodies,[43,44] vascular endothelial growth factor,[45] transferrin,[46] folic acid,[47] and mannose.[48]

Another targeting agent that can be used for the functionalization of NDs is hyaluronic acid (HA). This is a natural ubiquitous polysaccharide with excellent biocompatibility and biodegradability in the body, which can be recognized by cluster determinant 44 (CD44) receptors,[49,50] overexpressed on the surface of several tumour cells, such as breast, ovarian, liver and prostate cancer cells.[51,52] Although the high specificity of HA towards CD44 receptors has been proved for a broad range of nanoparticles,[53–55] research on the derivatization of NDs with HA has been limited. Yun et al. developed ND-based nanoparticles incorporating HA and a photosensitive molecule for photodynamic and photothermal tumour therapy, highlighting the selective ND uptake by HeLa cells due to the presence of HA.[56] Han et al. successfully attached HA on fluorescent NDs, delving into particle capabilities for liver-targeted molecular imaging. Through both in vitro and in vivo experiments, they demonstrated specific delivery of HA–ND conjugates to liver cells. Their work also showed the safety, biocompatibility, and imaging capability of these HA conjugates assessed through in vivo fluorescence lifetime measurements.[57] Both the works described are based on covalent bonded hyaluronic acid on a diamond surface obtained through advanced and complex chemical pathways. On the other hand, Cui et al. focused on developing ND-based theranostic platforms for triple-negative breast cancer treatment. They achieved ND functionalization through noncovalent bonding involving electrostatic interactions for coating NDs with a protamine sulphate layer. The proposed multi-step approach guarantees the adsorption of HA onto a protamine sulphate layer through charge complexation. In one study, curcumin and a photosensitive compound were encapsulated within the NDs,[58] while another study involved ND loading with the anticancer drug doxorubicin through electrostatic interactions.[59] In both cases, the developed nanosystems were characterized by uniform dimensions, high loading efficiency, excellent biocompatibility, and colloidal stability, showing prevalent localization in the tumour cells, thus evidencing the high potentiality of HA-functionalized NDs for the investigated application.[58,59] Lastly, Chernysheva et al. recently confirmed that the adsorption of miramistin on NDs enhances the adsorption of HA. This exploration introduces an alternative strategy for ND functionalization with HA, suggesting potential advancements in the field of drug nanocarriers.[60]

Due to the promising results from the aforementioned studies, the present investigation aims to explore a novel and smarter system for functionalizing NDs with HA through a non-covalent approach. Here, we demonstrate, for the first time, the successful functionalization of NDs with a conjugate of HA and 1,2-dimyristoyl-sn-glycero-3-phosphoethanolamine (HA/DMPE). This process showcases the selective internalization of functionalized particles into cancer cells that overexpress CD44 receptors, highlighting the potential for tracking these particles due to the fluorescence properties of NDs.

The targeting efficacy of HA/DMPE conjugates towards CD44-overexpressing cancer cells has previously been reported by our group for carbon nano-onions[61] and carbon nanotubes.[62] Functionalization not only imparts cell specificity to the nanoconstructs, but also enhances their dispersion in aqueous media. In this study, NDs were functionalized with a 200 kDa HA/DMPE conjugate using a ND : HA/DMPE ratio of 5 : 1. The characterization of the particles was conducted through diffuse reflectance Fourier transform infrared spectroscopy, Raman spectroscopy, and photoluminescence spectroscopy to gather information on the efficacy of the functionalization process. Scanning electron microscopy was employed to evaluate the size distribution of the dry particles, while Dynamic Light Scattering (DLS) and zeta potential measurements were utilized to evaluate the nanoparticles' behaviour in a water-based medium.

Furthermore, we assessed the ND biocompatibility and uptake mediated by CD44 receptors in three different models of human adenocarcinoma cells by performing cytofluorometric assay and confocal microscopy.

Results and discussion

ND sample preparation

The NDs considered in this study are MSY 0–0.1 purchased from Pureon and are characterized by different surface features. The samples were labelled as ND_{Ann}, ND_{Ox}, and ND_H, according to the various thermal treatments they underwent, which are detailed in the Experimental section and in Fig. S1 in the ESI.† ND_{Ann} were subjected solely to an annealing process under nitrogen flow. On the other hand, ND_{Ox} underwent annealing followed by oxidation in air, whereas ND_H experienced a sequential treatment involving annealing, oxidation and hydrogenation under hydrogen flux. The annealing and thermal processes ending with hydrogenation were intended to promote surface hydrophobicity by fostering the

formation of C–H terminations,[63,64] while post-annealing oxidation was performed to endow the ND surface with hydrophilic character through the establishments of oxygenated moieties.[65]

All the samples were non-covalently functionalized with a HA/DMPE conjugate. The conjugate was obtained by linking the phospholipid to HA *via* an amidic bond in the presence of a soluble carbodiimide derivative to give a product in which the phospholipid amino group is randomly linked to the carboxylic residues of HA.[62,66] After the dispersion of NDs in water for 90 min of bath sonication, the HA/DMPE conjugate previously solubilized in water was added and bath sonicated for further 90 min (Fig. S2†). The NDs were purified by centrifugation and a carbazole assay was performed to detect any amount of the non-covalently bound conjugate. The colorimetric assay confirmed that all the HA/DMPE was adsorbed onto the ND surface. Upon functionalization, ND_{Ann}, ND_{Ox}, and ND_H were respectively labelled as HA–ND_{Ann}, HA–ND_{Ox}, and HA–ND_H, as also reported in the Experimental section and in Fig. S1.†

ND characterization

Prior to evaluating ND behaviour in the cellular environment, to gain insights into the physical and chemical properties of both non-functionalized and hyaluronated samples, comprehensive material characterization was performed employing Diffuse Reflectance Infrared Fourier Transform (DRIFT) spectroscopy, Raman spectroscopy, Scanning Electron Microscopy (SEM), Dynamic Light Scattering (DLS) and photoluminescence (PL) spectroscopy.

To investigate sample's surface chemistry, assessing the success of thermal processes in the modifications of the ND surface and the effectiveness of the non-covalent functionalization with the HA-based conjugate, a DRIFT spectroscopy study was performed (Fig. 1a).

The DRIFT spectrum of ND_{Ann} reveals distinctive features in the 3000–2800 cm^{-1} spectral range, corresponding to the asymmetric and symmetric stretching of C–H bonds.[67] On the

other hand, no bands related to ν(O–H) stretching of the surface adsorbed water and hydroxyl groups appear between 3700 cm^{-1} and 3000 cm^{-1}.[68] Furthermore, only a faint signal at 1705 cm^{-1} can be detected in the ν(C=O) region.[69] These findings underscore the efficacy of the annealing treatment in forming C–H moieties on the ND_{Ann} surface, thus imparting it a hydrophobic behaviour. In contrast, the DRIFT spectrum of ND_{Ox} is characterized by a broad ν(O–H) band, along with a prominent and complex signal at 1800 cm^{-1}, which is attributed to the C=O stretching in various surface functionalities, encompassing esters, carboxylic acids, acid anhydrides and lactones.[69,70] Notably, the feature at 1705 cm^{-1} and the signals of C–H stretching are also present in the DRIFT spectrum of ND_{Ox}. However, the intensity of the former is higher in the case of ND_{Ox} compared to ND_{Ann}, while the opposite holds true for the latter. All such observations highlight that the oxidation process successfully resulted in the establishment of surface oxygenated moieties, thus rendering the surface of ND_{Ox} highly hydrophilic. This is further supported by the appearance of a series of new bands in the spectral region between 1500 cm^{-1} and 1300 cm^{-1}, ascribed to epoxide and ketone vibrations,[69,70] in addition to the visible shoulder at 1630 cm^{-1}, attributed to the water bending mode.[64,71] The DRIFT spectrum of ND_H is similar to the one of ND_{Ann}, being characterized by the absence of the ν(O–H) bands, as well as the presence of the main signals due to oxygen-containing moieties at 1800 cm^{-1} and in the 1500–1300 cm^{-1} range. Remarkably, it can be noted that the signals in the C–H stretching range are enhanced for ND_H with respect to the DRIFT spectrum of ND_{Ann}. The previously discussed features reveal the effectiveness of the hydrogenation process in forming surface C–H bonds, thus giving to the ND_H surface a hydrophobic character.

Before delving into the DRIFT analysis of the functionalized NDs, examination of HA alone was carried out with the purpose to determine distinctive markers for assessing the presence of the molecule on the surface of the functionalized samples. The HA spectrum is characterized by a broad band centred at 3390 cm^{-1}, associated with stretching vibrations of hydrogen bonded O–H. This is accompanied by a weak shoulder at *ca.* 3100 cm^{-1}, assigned to N–H vibrations, and by signals in the 3000–2800 cm^{-1} range, due to ν(C–H).[72] Additionally, several complex bands appear in the 1750–1500 cm^{-1} spectral region, assigned to amides I and II and the vibrations of various carbonyls and carboxyls.[73] Moreover, the broad signal extending between 1200 cm^{-1} and 1000 cm^{-1} gathers C–O stretching vibrations in alcohols and the antisymmetric C–O–C stretching in glycosidic groups.[73]

The comparative analysis between the DRIFT spectra of the hyaluronated NDs and those of the non-functionalized samples reveals discernible alterations in the shape of the characteristic bands of the latter upon derivatization. Substantial modifications are indeed evident in the C–H stretching bands when comparing HA–ND_{Ann} with ND_{Ann} and HA–ND_H with ND_H. Similarly, relevant changes can be observed in the O–H and C=O stretching signals when exam-
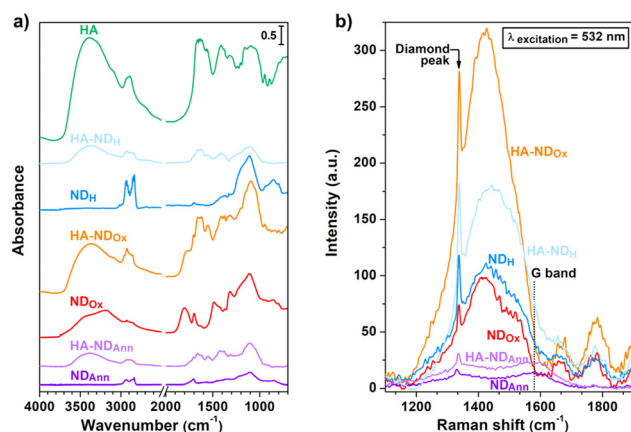

Fig. 1 (a) DRIFT spectra of the NDs and HA. (b) NDs Raman spectra obtained after baseline subtraction.

ining HA–ND$_{Ox}$ with respect to ND$_{Ox}$. The spectral comparison between the functionalized NDs with the NDs prior to derivatization also displays the appearance of additional features in the former. Such extra bands are the same in HA–ND$_{Ann}$, HA–ND$_{Ox}$ and HA–ND$_H$ and correspond to the signals detected for HA, which have been discussed above. Notably, ν(O–H) signals appear in HA–ND$_{Ann}$ and HA–ND$_H$, which are not present in ND$_{Ann}$ and ND$_H$. Moreover, C–H stretching bands are more pronounced in the DRIFT spectrum of HA–ND$_{Ox}$ with respect to the one of ND$_{Ox}$. Further confirmation of the correlation between the DRIFT features of ND samples and successful functionalization is evident in Fig. S3,† where a series of DRIFT spectra collected at decreasing HA/DMPE : ND ratios (1 : 10 and 1 : 15) are presented. As expected, the intensity of the bands attributed to HA decreases for the nanoparticles functionalized with a lower amount of the conjugate. These observations suggest the effective anchoring of HA to the nanodiamond surface.

With the aim of examining the structures of various samples and monitoring any potential structural perturbations to the NDs arising from the introduction of functionalization, Raman spectroscopy was performed and the corresponding results are presented in Fig. 1b. The Raman spectra of the samples all exhibit the first-order Raman peak of diamond,[74] while the G-band is observable only in the Raman spectra of ND$_{Ann}$ and HA–ND$_{Ann}$, appearing as a weak signal at 1580 cm^{-1}.[74] The latter observation indicates the formation of some graphite during the annealing treatment, suggesting at the same time its removal through oxidation and hydrogenation processes, as also documented in prior studies.[64,65] Notably, the Raman spectra of ND$_{Ox}$, HA–ND$_{Ox}$, ND$_H$, and HA–ND$_H$ reveal a signal at 1405 cm^{-1} overlapped with a broad shoulder, along with additional features at above 1600 cm^{-1}. These signals are not related to Raman scattering; instead, they arise from the photoluminescence of NV centers (further details concerning the photoluminescence properties of NDs are presented in the discussion of Fig. 4, displaying the photoluminescence spectra of the samples). Specifically, the feature at 1405 cm^{-1}, corresponding to 575 nm on the wavelength scale, is associated with the zero-phonon line of NV^0 centers, while the other peaks are phonon replicas due to the interaction between phonon states and electronic transitions.[74] It can be observed that the spectral features of ND$_{Ann}$, ND$_{Ox}$ and ND$_H$ are conserved in the Raman spectra of their functionalized counterparts, namely HA–ND$_{Ann}$, HA–ND$_{Ox}$ and HA–ND$_H$, meaning that the association of HA does not induce structural alterations to the NDs, not changing the diamond and graphite contents of the original particles.

To explore the characteristics of the ND samples in terms of median particle size, SEM and DLS analyses were carried out. SEM was employed to gain insights into the size distribution of the NDs in their dry state, as well as for analyzing their morphology. On the other hand, DLS characterized the particle dimensions in an aqueous environment, thus offering complementary information to the ones collected through SEM micrographs, in addition to the data regarding dispersibility

and stability in solution, which are crucial parameters for the application of the NDs in cellular context.

The size distributions of NDs obtained from SEM images are shown in Fig. 2a–c for the non-functionalized particles and in Fig. 2d–f for the functionalized ones. Median size diameters (D_{med}) for ND$_{Ann}$, ND$_{Ox}$, and ND$_H$ are respectively 53 nm, 55 nm and 53 nm with a corresponding standard deviation (σ) of 10 nm, 10 nm and 9 nm. These values align consistently with each other and with the dimensions specified by the producer (D_{med} = 50 nm ± 10 nm), indicating no appreciable influence of thermal treatments on the ND dimensions. Median size diameter values of the functionalized particles are 54 nm for HA–ND$_{Ann}$, 55 nm for HA–ND$_{Ox}$ and 52 nm for HA–ND$_H$ with a standard deviation equal to 10 nm, 10 nm and 8 nm, respectively. Notably, such values closely mirror those of their non-hyaluronated equivalents. Fig. 2 also shows details from the SEM micrographs of NDs. The pictures demonstrate that all the NDs exhibit irregular and jagged geometries, a distinctive feature preserved across both non-functionalized and functionalized samples. The collective results from both shape analysis and size distribution thus show that the functionalization has essentially no discernible impact on the geometry and the dimensions of the NDs in their dry state.

The median particle size and zeta potential of NDs and HA–NDs dispersed in water were analyzed by DLS after sonicating the prepared solution for 180 minutes using a sonicator bath at a frequency of 40 kHz. After aggressive sonication, the median diameter of the bare NDs closely matches the primary particle size, confirming that a negligible quantity of aggregates is present in the solution. This is a crucial aspect, as these ND solutions represent an intermediate step for the preparation of hyaluronated ones. Only ND$_H$, however, was confirmed to be less dispersible in water due to the hydrophobic nature of the hydrogenation termination, as demonstrated by the higher diameter and PDI compared to other bare NDs. As shown in Table 1, after modification with the HA/DMPE conjugate, the hydrodynamic median diameter of NDs (ND$_{Ann}$ and ND$_{Ox}$) does not change, but the zeta potential was more negative, due to the HA carboxyl groups, indicating the successful modification of the outer surface of the NDs.

The colloidal stability of the NDs is an important parameter for their biomedical applications, thus the stability of HA–NDs in RPMI 1640 + 10% FBS and water was evaluated. The size and zeta potential of the samples remained stable over 72 hours, indicating good stability in both water and cell medium (data not shown), while the unconjugated sample precipitated at the bottom of the container after a few hours. NDs in the presence of unconjugated 200 kDa HA were also prepared as a reference to compare the effect of the HA/DMPE conjugate with the one of the free HA in water. Fig. 3 shows the different behaviours of NDs in water immediately after dispersion and over one month at room temperature. HA–NDs were well-dispersed and stable without aggregation and any differences in median diameter and zeta potential values. On the other hand, NDs in the presence of unconjugated HA showed aggregation after one month.
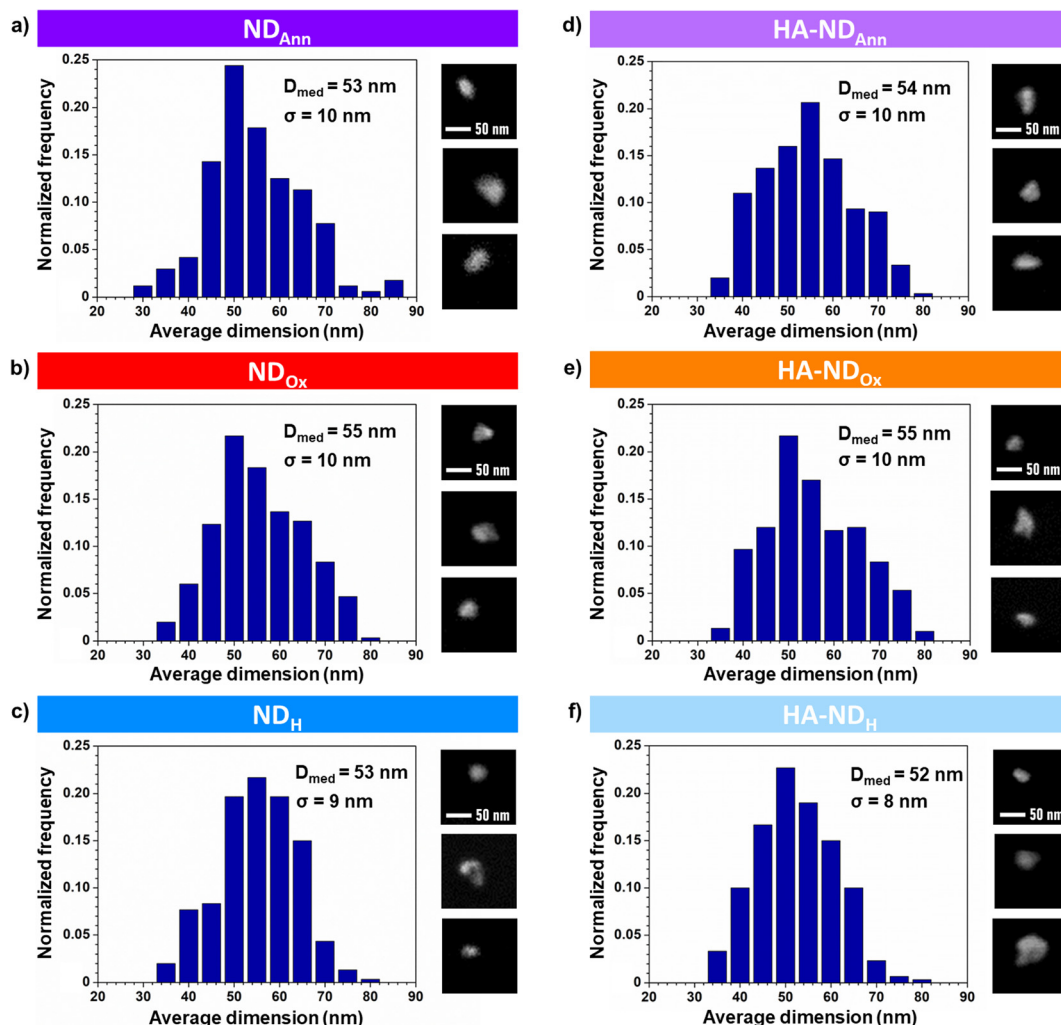
Fig. 2 Size distributions of the NDs derived from SEM images. Particle size histograms were constructed based on 300 NDs from 3–4 micrographs, except for ND_{Ann}, where the distribution was derived from 168 NDs. Details from SEM micrographs showing ND particles are also presented. (a) ND_{Ann}, (b) ND_{Ox}, (c) ND_H, (d) $HA–ND_{Ann}$, (e) $HA–ND_{Ox}$, and (f) $HA–ND_H$.

Table 1 Physico-chemical characterization of NDs ($n = 5$)

Sample	Median diameter (nm ± S.D.)	Polydispersity index (PDI)	Zeta potential (mV ± S.D.)
ND_{Ann}	59 ± 4	0.180	−22.6 ± 0.3
$HA–ND_{Ann}$	59 ± 1	0.166	−33.7 ± 0.9
ND_{Ox}	59 ± 4	0.122	−37.5 ± 3.1
$HA–ND_{Ox}$	59 ± 5	0.153	−45.8 ± 0.5
ND_H	80 ± 12	0.214	−20.1 ± 0.7
$HA–ND_H$	69 ± 6	0.119	−34.9 ± 0.3

These results confirm that the HA/DMPE conjugate confers excellent dispersibility and stability to ND preparations.

In order to investigate the photoluminescence (PL) properties of the NDs, playing a key role in their visualization in cells, the samples were analyzed by means of PL spectroscopy. The PL spectrum was collected also for the sole conjugate to assess its potential contributions to a reduction of particle

intrinsic fluorescence through any quenching effect. PL spectra of the samples are presented in Fig. 4, where the wavelength range highlighted by the black-contoured rectangle corresponds to the region reported in Fig. 1b in Raman values, since it displays features not only due to PL effects, but also arising from Raman scattering, as examined above (see the discussion of Fig. 1b). The PL spectra of NDs are all characterized by a broad band extending from 600 nm to 780 nm, which can be ascribed to the superposition of the phonon sidebands of NV^0 and NV^- centers, covering the 600–750 nm and the 650–750 nm wavelength range, respectively.[37] In the PL spectra of ND_{Ox}, $HA–ND_{Ox}$, ND_H, and $HA–ND_H$, signals corresponding to the zero-phonon lines of both types of NV centers are discernible. In particular, the one at 638 nm is associated with NV^- centers, while the one at 575 nm, falling in the contoured region and corresponding to 1405 cm^{-1} on the Raman shift scale, is ascribed to NV^0 centers,[37] as already discussed above. Observing together the PL spectra of the non-functionalized
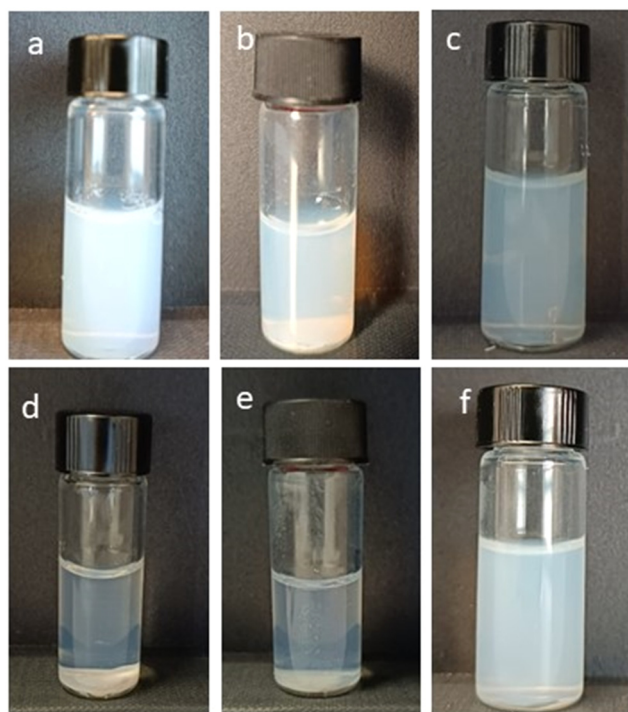
Fig. 3 Representative images of the NDs obtained immediately after dispersion (a–c) and after one month (d–f): (a and d) unconjugated HA–ND$_{Ox}$; (b and e) ND$_{Ox}$; and (c and f) HA–ND$_{Ox}$.
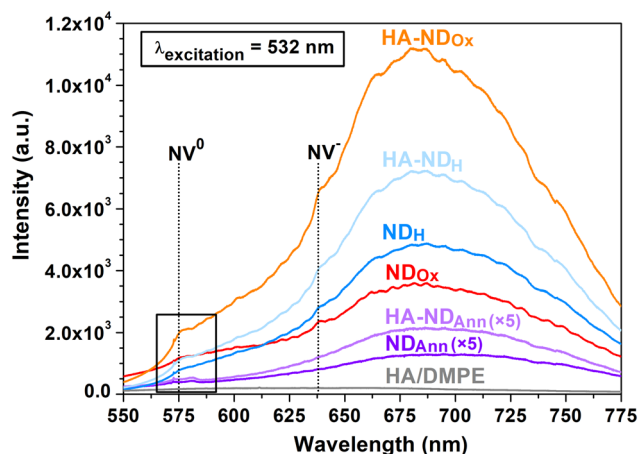

Fig. 4 Photoluminescence spectra of the NDs and the HA/DMPE conjugate. The PL spectra of ND$_{Ann}$ and HA–ND$_{Ann}$ are multiplied by a factor of five. The black rectangle identifies the region highlighted in Fig. 1b.

NDs, it can be noted that the fluorescence of ND$_{Ox}$ is increased compared to ND$_{Ann}$, and ND$_H$ exhibits even higher fluorescence than ND$_{Ox}$. Such a trend is likely due to the elimination of graphitic phases formed upon annealing through oxidation and combined oxidation + hydrogenation processes, as also suggested by the analysis of Raman spectra. Graphitic phases have indeed been reported to have a quenching effect

on the PL of NV centers[75] and hence their reduced presence should enhance the fluorescence of the NDs.

A noteworthy observation for HA–ND$_{Ann}$, HA–ND$_{Ox}$, and HA–ND$_H$ is the presence of luminescence, comparable to or even increased compared to that of their non-functionalized counterparts. The influence of the HA-based conjugate on optical spectral features can be deemed insignificant, as demonstrated by the photoluminescence spectrum of the pure conjugate, which exhibits no detectable new PL bands or peaks. The key finding emerging from the analysis of PL spectra is thus the preservation of particle fluorescence upon association, indicating that NDs continue to be well-suited agents for cellular imaging applications.

Taken together, all these data suggest the efficacy of our approach, which offers distinctive advantages over others reported in the literature for coating NDs with HA. In fact, these require some steps to obtain modified NDs, either involving the formation of a covalent bond between the ND-functional groups and HA or a two-step assembly strategy through the preliminary modification of NDs with protamine sulfate or miramistin. In contrast, our method streamlines the HA anchoring process, offering a more straightforward route for decorating NDs with HA, regardless of their different starting surface terminations.

ND cytotoxicity

First, we compared the cytotoxicity of different formulations of non-functionalized (ND$_{Ann}$, ND$_H$, ND$_{Ox}$) and HA-functionalized NDs (HA–ND$_{Ann}$, HA–ND$_H$ and HA–ND$_{Ox}$) across three pairs of cancer cell lines of pancreatic, breast and lung origin, which are three of the most common and aggressive cancer types. Each pair contained one cell line with low levels of CD44 and the second one with high levels of the receptor, respectively (Fig. S4†), to allow a better comparison between the effects of plain and HA-functionalized NDs. Dose- and time-dependent experiments suggested a good biocompatibility of all types of NDs across the different cancer cell lines. Indeed, even at the highest concentration (20 µg ml^{-1}) and at the most prolonged time (72 h), the reduction in cell viability was not >30% (see Fig. 5 and Fig. S5†). This experimental set demonstrates that NDs in all their formulations do not exert an appreciable cytotoxicity, therefore they could be proposed as safe carriers of chemotherapeutic drugs as future development. The not significant differences in terms of cytotoxicity between the cancer cell lines of different origins and histotypes within the same tumor type indicate that the good biocompatibility of ND was not cell line- or tumor-dependent.

ND uptake

We measured the intracellular uptake of different ND formulations at the same non-cytotoxic concentrations, exploiting the intrinsic fluorescence of NDs. By the fluorimetric analysis of the intracellular fluorescence, we observed a time- and dose-dependent uptake of NDs. For non-decorated NDs, the intracellular retention at 24 h followed this rank order:
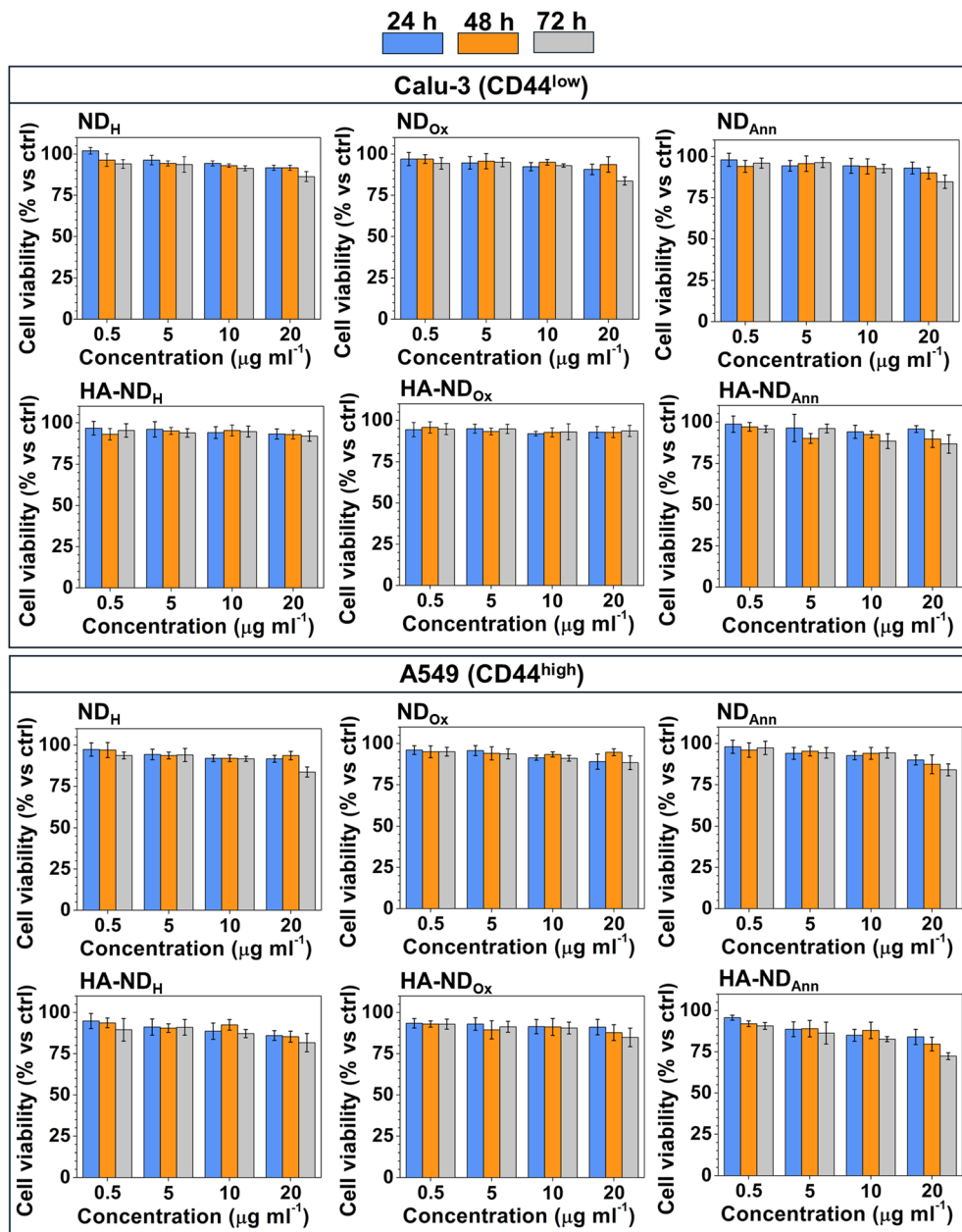
Fig. 5 Cell viability at 24, 48 and 72 h in human non-small cancer cell lines, Calu-3 and A549, incubated with ND_{Ann}, ND_H, ND_{Ox}, HA–ND_{Ann}, HA–ND_H and HA–ND_{Ox} at the indicated concentration by a chemiluminescence-based assay in triplicate ($n = 3$ independent experiments). Data are means + SD.

$ND_{Ann} \geq ND_H \geq ND_{Ox}$, independently from the surface level of CD44 (Fig. 6).

The slow time- and dose-dependent increase, without significant differences in the uptake between the different ND formulations, is indicative of a passive endocytosis of NDs in different cell types. The presence of the negative charge of the oxygenated groups in ND_{Ox}, deprotonated at the physiological pH, may render the passive diffusion of the NDs less efficient; indeed, in Calu-3, PANC-1 and MDA-MB-231 cells, ND_{Ox} was less taken up by the cells. The different behaviours may be explained by the different patterns of surface charge, due to

glycolipids and glycoproteins, that can make the entry of NDs more difficult because of electrostatic repulsion events. In low-CD44 surface level cells, we observed a comparable yet slightly enhanced uptake of HA–NDs compared to their non-functionalized counterparts. This phenomenon could be attributed to the general facilitation of cellular uptake conferred by ND surface coatings, as for instance observed in the case of zwitterionic moieties.[76] However, the observed increase also hints at the role of HA in promoting NDs internalization through interaction with CD44 receptors by facilitating receptor-mediated endocytotic pathways. Although the endocytosis
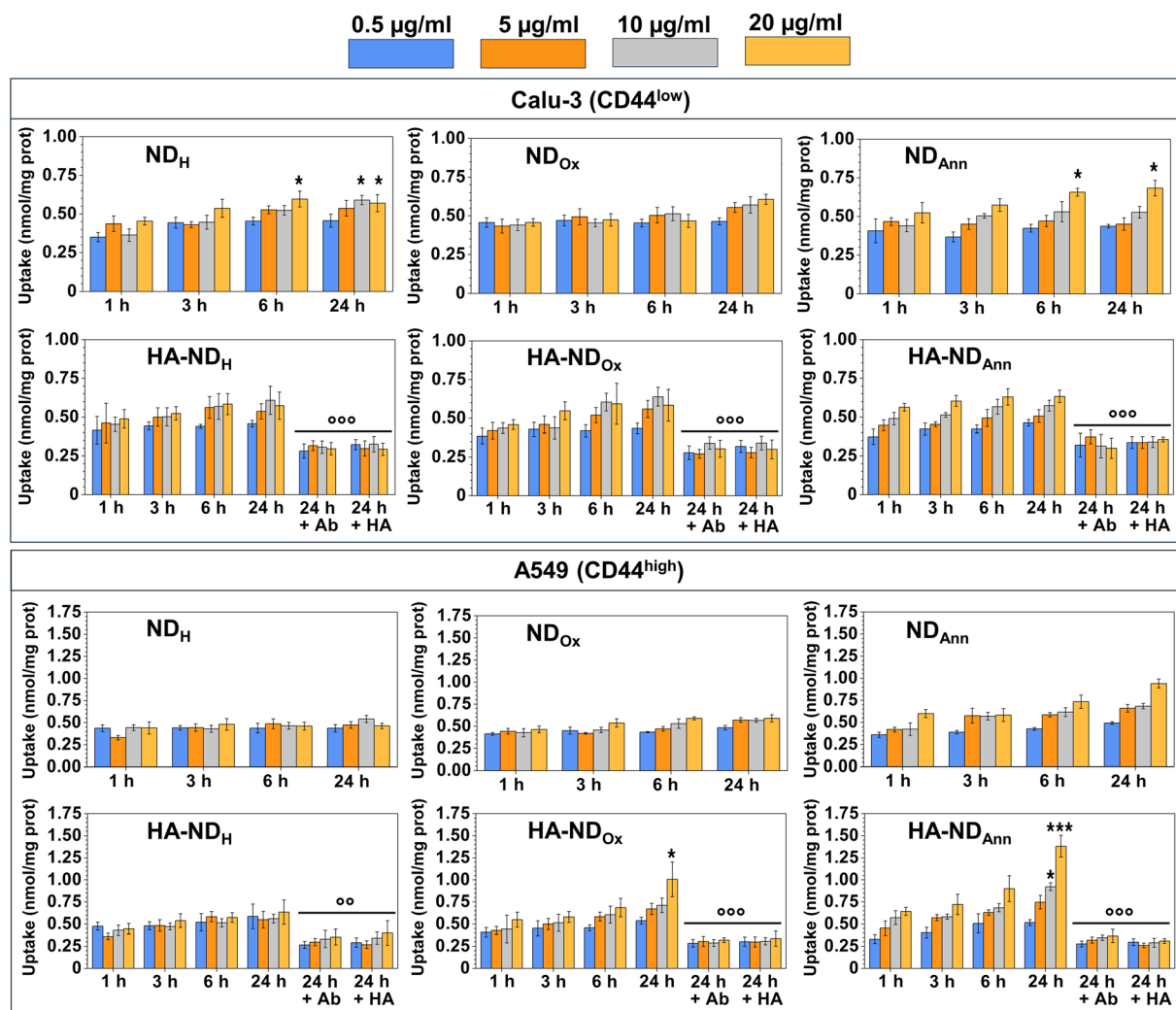
Fig. 6 Uptake of ND_{Ann}, ND_H, ND_{Ox}, HA–ND_{Ann}, HA–ND_H and HA–ND_{Ox} at the indicated concentrations after 1, 3, 6, and 24 h in human non-small cancer cell lines, Calu-3 and A549, by a fluorimetry-based assay in triplicate (n = 3 independent experiments). When indicated, an anti-CD44 neutralizing antibody (Ab, diluted 1/100) or 100 μM hyaluronic acid (HA) was co-incubated. Data are the means + SD. $*p < 0.05$, $***p < 0.001$: ND fluorescence $vs.$ cell autofluorescence; $\circ\circ p < 0.01$, $\circ\circ\circ p < 0.001$: ND fluorescence in cells treated with Ab/HA $vs.$ ND fluorescence in the cells without Ab/HA.

of HA-functionalized NDs was dependent on CD44-mediated endocytosis, as demonstrated by a significant reduction in the uptake in the presence of a CD44-blocking antibody or an excess of HA, the impact of the CD44-mediated route in the endocytosis of NDs seems equivalent to the impact of an unspecific endocytosis (Fig. S6†). Interestingly, in CD44-highly expressing A549 cells, the uptake of HA–ND_{Ann} and HA–ND_{Ox} was higher than the uptake of the corresponding non-functionalized NDs, indicating that in this cell model the endocytosis triggered by CD44 plays a preponderant role. Only HA–ND_H did not show a significantly higher uptake than ND_H; it is known that different tumors express different CD44 isoforms: the presence of a specific variant instead of another may facilitate or hamper the interaction between CD44 and HA–NDs. Therefore, a preliminary analysis of the amount and variants

of CD44 could be useful in determining the type of tumor that is the most suitable target for HA–NDs instead of bare NDs.

To prove that our NDs are good tools to label the CD44-positive cells, we analyzed the intracellular distribution of ND_{Ox} and HA–ND_{Ox} in A549 cells by confocal microscopy (Fig. 7). The intracellular accumulation was time dependent and appeared faster with ND_{Ox} than with HA–ND_{Ox}, in line with the different kinetics of entry dependent on the endocytosis route (unspecific $versus$ receptor-mediated endocytosis). ND_{Ox} reached indeed the maximum accumulation already after 3 h (data not shown), while HA–ND_{Ox} reached a comparable accumulation after 6 h. At 24 h, the amount was similar for both ND_{Ox} and HA–ND_{Ox}, indicating a likely saturation in the uptake mechanisms. Interestingly, the main site of intracellular localizations was the nuclear and the perinuclear regions.
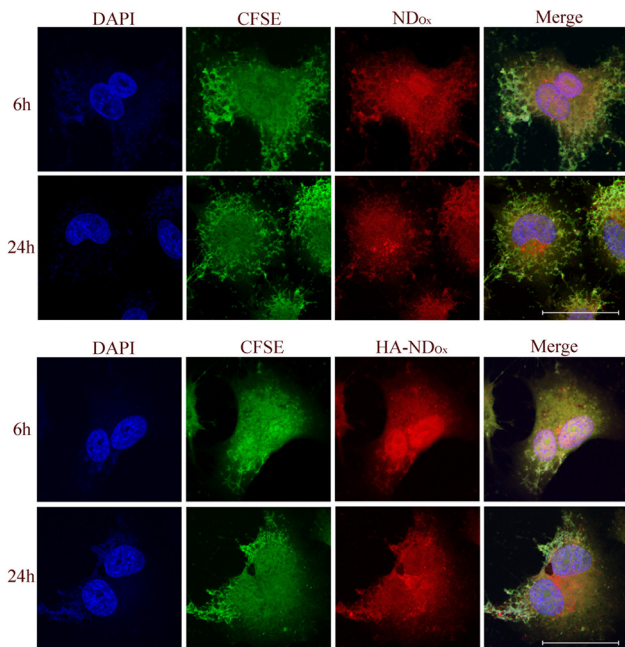
Fig. 7 Representative microscopy images of A549 cells incubated with 100 μg ml⁻¹ ND_{Ox} and $HA-ND_{Ox}$ for the indicated time. Photographs were taken with a Leica SP8 confocal microscope using a 60× objective. The scale bar is 50 μm.

Such distribution may suggest that NDs could be potentially good candidates as carriers of chemotherapeutic drugs that should be directed to the nucleus to exert their cytotoxic potential as gemcitabine, anthracyclines, taxanes, and platinum derivatives. These results may have a translational potential since these types of drugs are indeed the first-line treatment in pancreatic, breast and lung cancers, the three types of cancers analyzed in this work.

Conclusions

In the present work, we reported a new approach for the functionalization of NDs with HA based on non-covalent anchoring of the molecule on the particle surface. This was accomplished by exploiting a HA/DMPE conjugate, which was attached to NDs with different surface chemistry, obtained by performing annealing, oxidation and hydrogenation thermal treatments on commercial diamond nanocrystals. The ND samples were comprehensively characterized both before and after the functionalization in terms of surface chemistry, structure, size and optical properties.

DRIFT spectroscopy evidenced distinct changes in the surface functional groups induced on the NDs by thermal treatments, thus allowing us to prove the efficacy of each process in modifying ND surface chemistry. On the other hand, the comparison between the DRIFT spectra of non-functionalized NDs and their hyaluronated counterparts, showing significant alterations in the ND spectral features upon deriva-

tization, confirmed the successful anchoring of HA to the ND surface.

Functionalized nanoparticles exhibited enhanced dispersibility and stability in water while preserving the fluorescence properties of nitrogen vacancy colour centers. Biocompatibility assays across pancreatic, breast, and lung cancer cell lines indicated the safety of both non-functionalized and HA-functionalized ND formulations with no relevant differences observed among the cell lines of different origins and histotypes within the same tumor type. Fluorimetric analysis revealed the time- and dose-dependent uptake of NDs, primarily through passive endocytosis across various cell types, with HA-functionalized NDs showing similar uptake patterns in CD44-rich cells dependent on CD44-mediated endocytosis. Confocal microscopy further supported ND potential to target the nuclear regions of cancer cells expressing CD44, underscoring the promising potential of NDs as efficacious drug delivery nanocarriers, particularly for targeting pancreatic, breast, and lung cancers. The observed time-dependent intracellular accumulation, with preferential localization in the nuclear and perinuclear regions, not only elucidates the kinetics of ND uptake *via* different endocytosis pathways, but also highlights their suitability as vehicles for chemotherapeutic agents requiring nuclear targeting, thus suggesting the translational potential of these systems in cancer therapy.

Overall, we observed that NDs are safe nanoparticles that can be taken up by different cancer types. The presence of CD44 on the cancer cell surface offers the possibility of using HA-functionalized NDs that have the advantage of an active targeting, implying a higher delivery of the drug to the tumors over the non-tumor tissues. Also, CD44-poorly expressing cancers, however, could be easily targeted by the NDs, thanks to their good passive diffusion within cancer cells.

The next steps will be the application of NDs as drug nanocarriers loaded with chemotherapeutic drugs. Improving the drug delivery into pancreatic, breast and lung cancer, where chemoresistance is well documented at the clinical level,[77–79] is still an open challenge. Our approach can represent a step forward in this direction.

Experimental

ND sample preparation

The employed NDs are MSY 0–0.1 with a nominal median diameter of (50 ± 10) nm purchased from Pureon. Realized by means of grinding of HPHT diamond single crystals, they are classified as type Ib, having a nominal concentration of single substitutional nitrogen between 10 ppm and 100 ppm. NDs were processed with different thermal treatments in a tubular furnace to modify their surface, as represented in the scheme of Fig. S1 in the ESI.† NDs were subjected to an annealing process under nitrogen flow, which was performed at 800 °C for 2 h. This had the purpose of standardizing the ND surface through the elimination of surface functionalities, concurrently graphitizing amorphous carbon components present on
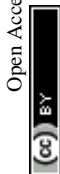
particle surface without damaging the diamond core. After the treatment with nitrogen, on a part of the annealed powders, an air oxidation process for 36 h at 500 °C was performed with the aim of purifying NDs from graphitic layers thanks to the selective removal of sp[2] carbon, while simultaneously decorating at the surface with oxygen-containing functional groups. A batch of the NDs subjected to the oxidation was further processed via a hydrogenation treatment under hydrogen flow for 3 h at 850 °C to promote the formation of hydrogen termination on the surface.

Preparation of HA/DMPE

The 200 kDa hyaluronic acid–1,2-dimyristoyl-sn-glycero-3-phosphoethanolamine (HA/DMPE) conjugate and the fluoresceinamine-labelled HA/DMPE conjugate (f-HA/DMPE) were synthesized as previously described.[62]

Non-covalent functionalization of NDs

The HA/DMPE conjugate was used for the non-covalent functionalization of NDs (HA–NDs). NDs were dispersed in MilliQ® water at a concentration of 0.5 mg ml^{-1} and bath sonicated for 90 min at 25 °C. Then, the amount of HA/DMPE to give a 5 : 1 NDs : HA/DMPE weight ratio was added to the ND suspension and bath sonicated for 90 min at 25 °C.

To remove the possible excess of HA/DMPE, the suspension was centrifuged at 11 000 rpm for 5 min and the percentage of HA on the supernatant was determined by the carbazole assay.[80]

The same experimental procedure was used for the functionalization of ND_{Ann} with the f-HA/DMPE conjugate for further cellular uptake experiments.

ND characterization

Diffuse reflectance infrared Fourier transform (DRIFT) spectroscopy. Diffuse Reflectance Infrared Fourier Transform (DRIFT) spectroscopy was carried out to investigate samples surface chemistry, allowing to check their successful modification through thermal treatments and conjugation with HA/DMPE. Each IR spectrum was recorded under dry air ambient conditions using a Bruker Vector 22 FTIR spectrometer, equipped with a mercury–cadmium–telluride detector, by averaging 64 acquisitions at 2 cm^{-1} spectral resolution. The collected reflectance values were successively converted in pseudo-absorbance (A) values, thanks to the relationship $A = -\log R$, where R represents the measured reflectance.

Raman and photoluminescence spectroscopy techniques. Raman spectroscopy and photoluminescence spectroscopy techniques were performed to investigate the structure of the NDs and their fluorescence optical properties derived from NV centers, respectively. NDs were dispersed in isopropanol and deposited on a silicon wafer for spectral collection. A Horiba Jobin Yvon HR800 Raman micro-spectrometer was employed to acquire both Raman and photoluminescence data. This was equipped with a 600 lines per mm diffraction grating, enabling to obtain a 3 cm^{-1} spectral resolution and a Peltier-cooled (−70 °C) CCD detector. The optical excitation was provided by

a continuous Nd-YAG solid-state 532 nm laser focused with a 20× objective, which allowed to probe a sample area of 10 × 10 μm^2 and a confocal depth of ∼3 μm. The laser power intensity incident on the sample was regulated to 0.178 mW through the insertion of a filter along the optical path. Notably, during data analysis, Raman spectra were obtained by subtracting the photoluminescence background to enhance the visibility of spectral features.

Scanning electron microscopy (SEM). Scanning Electron Microscopy (SEM) was employed to investigate the ND size distribution and their morphology. The examinations were carried out using an Inspect F™ scanning electron microscope with a field emission gun, operating in secondary electron (SE) detection mode at a 5 kV acceleration voltage under high-vacuum conditions (approximately 10^{-6} mbar pressure), which provided a spatial resolution of about 10 nm. To prepare the samples for imaging, NDs were dispersed in isopropanol and sonicated for 15 minutes using an Elmasonic S15H ultrasonic device (35 W ultrasonic power). Subsequently, droplets of the prepared ND suspensions were deposited onto silicon substrates and allowed to air-dry. Notably, the NDs under examination were intentionally left uncoated with metal to avoid potential morphological alterations, even though this choice might have introduced some charging effects.

For the analysis of size distribution, the ImageJ program was utilized. The dimensions of the nanocrystals were determined from the micrographs by manually tracing the contours of the projected areas of the NDs, considering only well-separated particles. Assuming a spherical nanoparticle shape, the obtained data were converted back to diameter values and particle size histograms were generated using an appropriate binning technique.

DLS and zeta potential measurements. The particle sizes and polydispersity indexes (PDI) of different NDs were measured at 25 °C using a Nanosizer (Zetasizer Pro, Malvern Inst., Malvern, UK). The selected angle was 173° and the measurement was performed after 1 : 10 dilution in MilliQ® water.

The surface charge was investigated via zeta potential measurement at 25 °C using the Smoluchowski equation and the Zetasizer Pro after 1 : 10 dilution of the suspensions in MilliQ® water. Each value reported is the average of three measurements.

The colloidal stability of functionalized NDs was assessed after 1 : 5 dilution in RPMI 1640 + 10% fetal bovine serum (FBS). The particle size and zeta potential were measured after 30 min, 24, 48 and 72 h incubation at 37 °C by diluting 1 : 2 in MilliQ® water. The colloidal stability of functionalized NDs dispersed in MilliQ® water was also evaluated at room temperature and the dispersions in water were also photographed immediately after sonication and over a 30-day period.

Cell line culture and characterization. Human pancreatic adenocarcinoma cells, Capan-1 and PANC-1, human breast cancer MCF-7 and MDA-MB-231 cells, and human non-small cell lung cancer Calu-3 and A549 cells were purchased from ATCC (Manassas, VA) and maintained in their respective medium (DMEM for Capan-1, PANC-1, and MCF-7, RPMI

16140 for MDA-MB-231 and Calu-3, and HAM's F12 for A549, all purchased from Invitrogen Life Technology, Milan, Italy) containing 1% v/v penicillin–streptomycin and 10% FBS (Merck, Milan, Italy). The surface amount of CD44, the receptor for HA, was evaluated by flow cytometry as previously described[81] using a Guava Millipore flow cytometer equipped with EasyCite software (Millipore, Bedford, MA).

Cytotoxicity. 1×10^4 cells were seeded into a 96-well white plate and incubated for 24, 48 and 72 h with fresh medium or medium containing 0.5, 5, 10, and 20 µg ml^{-1} ND$_{Ann}$, ND$_H$, and ND$_{Ox}$, either non-functionalized or HA-functionalized. Cell viability was measured using an ATPlite Luminescence Assay System (PerkinElmer, Waltham, MA) as per the manufacturer's instructions. The results were analyzed using a Synergy HT microplate reader (Bio-Tek Instruments, Winooski, VT). The luminescence units of the untreated cells were considered 100%; the luminescence units of the other experimental conditions were expressed as percentage *versus* untreated cells.

Uptake. 1×10^5 cells were seeded into a 96-well black plate and incubated for 1, 3, 6, or 24 h with 0.5, 5, 10, and 20 µg ml^{-1} ND$_{Ann}$, ND$_H$, and ND$_{Ox}$, either non-functionalized or HA-functionalized. When indicated, a saturating amount of blocking anti-CD44 antibody (#ab157107; Abcam, Cambridge, UK; diluted 1/100) or HA (100 µM) was added to the cells incubated with 20 µg ml^{-1} HA–NDs. The cells were washed twice with PBS and rinsed with 300 µl of PBS. The intracellular fluorescence, an index of liposome uptake, was measured using a Synergy HT microplate reader under λ excitation at 488 nm and λ emission at 580 nm. The cells were then detached with trypsin/EDTA, sonicated and used for the measure of intracellular protein contents. The results were expressed as fluorescence units (FU) per mg cellular protein.

Confocal microscopy. For immunostaining, A549 cells were grown on 22 mm cover glasses and then incubated as indicated in the Fig. 7 legend. After the incubation, the cells were stained with 0.5 µg ml^{-1} 5(6)-carboxyfluorescein diacetate and NHS ester (CFSE) in PBS for 10 min, and then washed once in PBS and fixed at RT with 4% paraformaldehyde (PFA) for 15 min. The cells were then permeabilized with 0.1% Triton-X-100 in PBS for 10 min and washed 3 times in PBS. Nucleus staining was performed with a DNA dye, DAPI (Merck), at 0.5 µg ml^{-1} in PBS for 10 min at RT and mounting was performed using Fluoromount™ Aqueous Mounting Medium (Merck). Images were acquired using a Leica SP8 confocal system with HyVolution 2 (Leica Microsystems) with a 60× objective and zoom 2×. All the images were analyzed by using Adobe Photoshop CS.

Statistical analysis. Data in the text and figures are provided as means ± SD. The results were analyzed by a one-way analysis of variance (ANOVA) and Tukey's test. $p < 0.05$ was considered significant.

Author contributions

Conceptualization: SA and FP; formal analysis: LM; investigation: SS, IA, PA, VB, JK and BZ; methodology: BS, SA, FP and CR; resources: BS, SA, FP and CR; supervision: SA and FP; validation: SS, IA, PA, VB, JK and BZ; writing – original draft: SS, CR and IA; writing – review and editing: SS, IA, PA, VB, JK, LM, BS, BZ, CR, SA and FP.

Conflicts of interest

There are no conflicts to declare.

Acknowledgements

Notes and references

1 V. V. Danilenko, *Phys. Solid State*, 2004, **46**, 595–599.
2 A. M. Panich, A. I. Shames, D. Mogilyansky, S. D. Goren and V. Y. Dolmatov, *Diamond Relat. Mater.*, 2020, **108**, 107918.
3 J.-P. Boudou, P. A. Curmi, F. Jelezko, J. Wrachtrup, P. Aubert, M. Sennour, G. Balasubramanian, R. Reuter, A. Thorel and E. Gaffet, *Nanotechnology*, 2009, **20**, 235602.
4 M. Frenklach, W. Howard, D. Huang, J. Yuan, K. E. Spear and R. Koba, *Appl. Phys. Lett.*, 1991, **59**, 546–548.
5 M. Alkahtani, J. Lang, B. Naydenov, F. Jelezko and P. Hemmer, *ACS Photonics*, 2019, **6**, 1266–1271.
6 J.-R. Bertrand, C. Pioche-Durieu, J. Ayala, T. Petit, H. A. Girard, C. P. Malvy, E. Le Cam, F. Treussart and J.-C. Arnault, *Biomaterials*, 2015, **45**, 93–98.
7 D. P. Mitev, A. M. Alsharabasy, L. Morrison, S. Wittig, C. Diener and A. Pandit, *Front. Bioeng. Biotechnol.*, 2021, **9**, 1–18.
8 A. Krueger and D. Lang, *Adv. Funct. Mater.*, 2012, **22**, 890–906.
9 Ashek-I-Ahmed, L. Gines, S. Mandal, C.-Y. Song, O. A. Williams, M. N. Sarmiento and C.-L. Cheng, *ACS Omega*, 2019, **4**, 16715–16723.
10 S. Sturari, V. Varzi, P. Aprà, A. Britel, N.-H. Amine, G. Andrini, E. Corte, G. Tomagra, L. Mino, P. Olivero and F. Picollo, *Surf. Interfaces*, 2023, **38**, 102831.
11 V. N. Mochalin, O. Shenderova, D. Ho and Y. Gogotsi, *Nat. Nanotechnol.*, 2012, **7**, 11–23.
12 C. Li, X. Zhang, E. F. Oliveira, A. B. Puthirath, M. R. Neupane, J. D. Weil, A. G. Birdwell, T. G. Ivanov, S. Kong, T. Gray, H. Kannan, A. Biswas, R. Vajtai, D. S. Galvao and P. M. Ajayan, *Carbon*, 2021, **182**, 725–734.
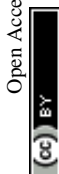
13 F. Picollo, L. Mino, A. Battiato, S. Ditalia Tchernij, J. Forneris, K. Martina, M. Sacco, S. Tagliapietra, E. Vittone, P. Olivero and A. Barge, *Diamond Relat. Mater.*, 2019, **91**, 22–28.

14 C.-C. Chou and S.-H. Lee, *Wear*, 2010, **269**, 757–762.

15 I. Neitzel, V. Mochalin, J. A. Bares, R. W. Carpick, A. Erdemir and Y. Gogotsi, *Tribol. Lett.*, 2012, **47**, 195–202.

16 Y. Zhang, J. R. Choi and S.-J. Park, *Composites, Part A*, 2017, **101**, 227–236.

17 Y. Zhang, K. Y. Rhee, D. Hui and S.-J. Park, *Composites, Part B*, 2018, **143**, 19–27.

18 Y. Song, H. Li, L. Wang, D. Qiu, Y. Ma, K. Pei, G. Zou and K. Yu, *Chem. Commun.*, 2016, **52**, 10497–10500.

19 H. Wang and Y. Cui, *Carbon Energy*, 2019, **1**, 13–18.

20 Y. Wu, M. N. A. Alam, P. Balasubramanian, A. Ermakova, S. Fischer, H. Barth, M. Wagner, M. Raabe, F. Jelezko and T. Weil, *Nano Lett.*, 2021, **21**, 3780–3788.

21 N. Norouzi, A. C. Nusantara, Y. Ong, T. Hamoh, L. Nie, A. Morita, Y. Zhang, A. Mzyk and R. Schirhagl, *Carbon*, 2022, **199**, 444–452.

22 H. Zhang, X. Chen and Z. Yin, *Adv. Quantum Technol.*, 2021, **4**, 2000154.

23 M. Radulaski, J. L. Zhang, Y. K. Tzeng, K. G. Lagoudakis, H. Ishiwata, C. Dory, K. A. Fischer, Y. A. Kelaita, S. Sun, P. C. Maurer, K. Alassaad, G. Ferro, Z. X. Shen, N. A. Melosh, S. Chu and J. Vučković, *Laser Photonics Rev.*, 2019, **13**, 1–14.

24 K. van der Laan, M. Hasani, T. Zheng and R. Schirhagl, *Small*, 2018, **14**, 1–17.

25 S. Chauhan, N. Jain and U. Nagaich, *J. Pharm. Anal.*, 2020, **10**, 1–12.

26 Y. Tian, A. C. Nusantara, T. Hamoh, A. Mzyk, X. Tian, F. Perona Martinez, R. Li, H. P. Permentier and R. Schirhagl, *ACS Appl. Mater. Interfaces*, 2022, **14**, 39265–39273.

27 Y. Zamani, A. Zareein, L. Bazli, R. NasrAzadani, B. P. Mahammod, S. Nasibi and A. M. Chahardehi, *J. Compos. Compd.*, 2020, **2**, 215–227.

28 M. Adel, P. Keyhanvar, I. Zare, Z. Tavangari, A. Akbarzadeh and M. Zahmatkeshan, *J. Drug Delivery Sci. Technol.*, 2023, **90**, 105130.

29 G. Petrini, G. Tomagra, E. Bernardi, E. Moreva, P. Traina, A. Marcantoni, F. Picollo, K. Kvaková, P. Cígler, I. Pietro Degiovanni, V. Carabelli and M. Genovese, *Adv. Sci.*, 2022, **9**, 2202014.

30 Y. Wu and T. Weil, *Adv. Sci.*, 2022, **9**, 2200059.

31 R. Grall, H. Girard, L. Saad, T. Petit, C. Gesset, M. Combis-Schlumberger, V. Paget, J. Delic, J. C. Arnault and S. Chevillard, *Biomaterials*, 2015, **61**, 290–298.

32 M. Kurzyp, H. A. Girard, Y. Cheref, E. Brun, C. Sicard-Roselli, S. Saada and J. C. Arnault, *Chem. Commun.*, 2017, **53**, 1237–1240.

33 V. Varzi, E. Fratini, M. Falconieri, D. Giovannini, A. Cemmi, J. Scifo, I. Di Sarcina, P. Aprà, S. Sturari, L. Mino, G. Tomagra, E. Infusino, V. Landoni, C. Marino, M. Mancuso, F. Picollo and S. Pazzaglia, *Int. J. Mol. Sci.*, 2023, **24**, 16622.

34 Y. Y. Hui, C. L. Cheng and H. C. Chang, *J. Phys. D: Appl. Phys.*, 2010, **43**, 374021.

35 N. Mohan, C. S. Chen, H. H. Hsieh, Y. C. Wu and H. C. Chang, *Nano Lett.*, 2010, **10**, 3692–3699.

36 W. W. W. Hsiao, Y. Y. Hui, P. C. Tsai and H. C. Chang, *Acc. Chem. Res.*, 2016, **49**, 400–407.

37 M. W. Doherty, N. B. Manson, P. Delaney, F. Jelezko, J. Wrachtrup and L. C. L. Hollenberg, *Phys. Rep.*, 2013, **528**, 1–45.

38 J. I. Chao, E. Perevedentseva, P. H. Chung, K. K. Liu, C. Y. Cheng, C. C. Chang and C. L. Cheng, *Biophys. J.*, 2007, **93**, 2199–2208.

39 C.-C. Fu, H.-Y. Lee, K. Chen, T.-S. Lim, H.-Y. Wu, P.-K. Lin, P.-K. Wei, P.-H. Tsao, H.-C. Chang and W. Fann, *Proc. Natl. Acad. Sci. U. S. A.*, 2007, **104**, 727–732.

40 S.-J. Yu, M.-W. Kang, H.-C. Chang, K.-M. Chen and Y.-C. Yu, *J. Am. Chem. Soc.*, 2005, **127**, 17604–17605.

41 J. Fang, H. Nakamura and H. Maeda, *Adv. Drug Delivery Rev.*, 2011, **63**, 136–151.

42 D. H. Jariwala, D. Patel and S. Wairkar, *Mater. Sci. Eng., C*, 2020, **113**, 110996.

43 B. M. Chang, H. H. Lin, L. J. Su, W. Der Lin, R. J. Lin, Y. K. Tzeng, R. T. Lee, Y. C. Lee, A. L. Yu and H. C. Chang, *Adv. Funct. Mater.*, 2013, **23**, 5737–5745.

44 D. Terada, S. Sotoma, Y. Harada, R. Igarashi and M. Shirakawa, *Bioconjugate Chem.*, 2018, **29**, 2786–2792.

45 M. D. Torelli, A. G. Rickard, M. V. Backer, D. S. Filonov, N. A. Nunn, A. V. Kinev, J. M. Backer, G. M. Palmer and O. A. Shenderova, *Bioconjugate Chem.*, 2019, **30**, 604–613.

46 M.-F. Weng, S.-Y. Chiang, N.-S. Wang and H. Niu, *Diamond Relat. Mater.*, 2009, **18**, 587–591.

47 B. Zhang, Y. Li, C. Fang, C. Chang, C. Chen, Y. Chen and H. Chang, *Small*, 2009, **5**, 2716–2721.

48 K. Kvakova, M. Ondra, J. Schimer, M. Petrik, Z. Novy, H. Raabova, M. Hajduch and P. Cigler, *Adv. Funct. Mater.*, 2022, **32**, 1–14.

49 G. Mattheolabakis, L. Milane, A. Singh and M. M. Amiji, *J. Drug Targeting*, 2015, **23**, 605–618.

50 F. Dosio, S. Arpicco, B. Stella and E. Fattal, *Adv. Drug Delivery Rev.*, 2016, **97**, 204–236.

51 C. Chen, S. Zhao, A. Karnad and J. W. Freeman, *J. Hematol. Oncol.*, 2018, **11**, 1–23.

52 M. Hassn Mesrati, S. E. Syafruddin, M. A. Mohtar and A. Syahir, *Biomolecules*, 2021, **11**, 1850.

53 J. Kim, M. Moon, D. Kim, S. Heo and Y. Jeong, *Polymers*, 2018, **10**, 1133.

54 Y. Liang, Y. Wang, L. Wang, Z. Liang, D. Li, X. Xu, Y. Chen, X. Yang, H. Zhang and H. Niu, *Bioact. Mater.*, 2021, **6**, 433–446.

55 M. C. de Paula, S. G. Carvalho, A. L. P. Silvestre, A. M. dos Santos, A. B. Meneguin and M. Chorilli, *Carbohydr. Polym.*, 2023, **320**, 121257.

56 T. H. Yun, G. Ahn, I. Choi, Y. Bae, K. Hwang, S. Kang and S. Choi, *Polym. Adv. Technol.*, 2020, **31**, 2990–2998.
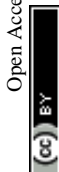
57 H. H. Han, H. Kang, S.-J. Kim, R. Pal, A. T. N. Kumar, H. S. Choi and S. K. Hahn, *RSC Adv.*, 2021, **11**, 23073–23081.

58 X. Cui, X. Deng, Z. Liang, J. Lu, L. Shao, X. Wang, F. Jia, Z. Pan, Q. Hu, X. Xiao, Y. Wu and W. Sheng, *Biomater. Sci.*, 2021, **9**, 3838–3850.

59 X. Cui, Z. Liang, J. Lu, X. Wang, F. Jia, Q. Hu, X. Xiao, X. Deng, Y. Wu and W. Sheng, *Nanoscale*, 2021, **13**, 13375–13389.

60 M. G. Chernysheva, A. V. Sinolits, V. S. Votyakova, A. G. Popov and G. A. Badun, *Mendeleev Commun.*, 2022, **32**, 501–503.

61 M. d'Amora, A. Camisasca, A. Boarino, S. Arpicco and S. Giordani, *Colloids Surf., B*, 2020, **188**, 110779.

62 S. Arpicco, M. Bartkowski, A. Barge, D. Zonari, L. Serpe, P. Milla, F. Dosio, B. Stella and S. Giordani, *Front. Chem.*, 2020, **8**, 1–12.

63 N. S. Xu, J. Chen and S. Z. Deng, *Diamond Relat. Mater.*, 2002, **11**, 249–256.

64 P. Aprà, L. Mino, A. Battiato, P. Olivero, S. Sturari, M. C. Valsania, V. Varzi and F. Picollo, *Nanomaterials*, 2021, **11**, 2740.

65 S. Osswald, G. Yushin, V. Mochalin, S. O. Kucheyev and Y. Gogotsi, *J. Am. Chem. Soc.*, 2006, **128**, 11635–11642.

66 C. Surace, S. Arpicco, A. Dufaÿ-Wojcicki, V. Marsaud, C. Bouclier, D. Clay, L. Cattel, J.-M. Renoir and E. Fattal, *Mol. Pharm.*, 2009, **6**, 1062–1073.

67 C. Barzan, L. Mino, E. Morra, E. Groppo, M. Chiesa and G. Spoto, *ChemCatChem*, 2017, **9**, 4324–4327.

68 L. Mino, Á. Morales-García, S. T. Bromley and F. Illas, *Nanoscale*, 2021, **13**, 6577–6585.

69 T. Petit and L. Puskar, *Diamond Relat. Mater.*, 2018, **89**, 52–66.

70 M. Acik, G. Lee, C. Mattevi, A. Pirkle, R. M. Wallace, M. Chhowalla, K. Cho and Y. Chabal, *J. Phys. Chem. C*, 2011, **115**, 19761–19781.

71 L. Mino, C. Negri, R. Santalucia, G. Cerrato, G. Spoto and G. Martra, *Molecules*, 2020, **25**, 4605.

72 R. Gilli, M. Kacuráková, M. Mathlouthi, L. Navarini and S. Paoletti, *Carbohydr. Res.*, 1994, **263**, 315–326.

73 K. Haxaire, Y. Maréchal, M. Milas and M. Rinaudo, *Biopolymers*, 2003, **72**, 10–20.

74 A. M. Zaitsev, *Optical Properties of Diamond*, Springer, 2001.

75 B. R. Smith, D. Gruber and T. Plakhotnik, *Diamond Relat. Mater.*, 2010, **19**, 314–318.

76 A. Sigaeva, V. Merz, R. Sharmin, R. Schirhagl and A. Krueger, *J. Mater. Chem. C*, 2023, **11**, 6642–6650.

77 M. Ashrafizadeh, K. Luo, W. Zhang, A. Reza Aref and X. Zhang, *Environ. Res.*, 2024, **240**, 117443.

78 K. Bhise, N. S. Gavande and A. K. Iyer, *Drug Discovery Today*, 2023, **28**, 103761.

79 P. Malik, R. Rani, R. Solanki, V. H. Patel and T. K. Mukherjee, *Explor. Targeted Anti-Tumor Ther.*, 2023, 850–895.

80 T. Bitter and H. M. Muir, *Anal. Biochem.*, 1962, **4**, 330–334.

81 M. E. Cano, D. Lesur, V. Bincoletto, E. Gazzano, B. Stella, C. Riganti, S. Arpicco and J. Kovensky, *Carbohydr. Polym.*, 2020, **248**, 116798.